Spatially distributed and simultaneous wind measurements with a fleet of small quadrotor UAS

Spatially distributed and simultaneous wind measurements with a fleet of small quadrotor UAS

Tamino Wetz [1], Norman Wildmann [1]

[1] Deutsches Zentrum für Luft- und Raumfahrt e.V., Institut für Physik der Atmosphäre, Oberpfaffenhofen, Germany

E-mail: tamino.wetz@dlr.de

Abstract. The understanding of micro-scale flow in the atmospheric boundary layer is one major challenge in wind energy research. Besides the broad possibilities of numerical simulations, experimental data are necessary for tests of the flow conditions within a wind farm under real conditions. In wind energy and atmospheric science, a variety of measurement devices exist for measuring the wind speed. We propose a measurement system that enables completely flexible simultaneous wind measurements using a fleet of multirotor unmanned aircraft systems (UAS). This approach is validated through a two-week measurement campaign at the boundary layer field site Falkenberg of the German National Meteorological Service (DWD). The wind speed is calculated from UAS motions in hover state without additional wind sensors. The measurements are calibrated and validated against sonic anemometers mounted at a 99 m mast. The capability of highly accurate spatial distributed wind measurement with an improved wind algorithm is proven by a root mean square error (RMSE) of 0.25 ms^{-1} for the horizontal wind speed and $< 5°$ for the wind direction. Further, turbulence measurements are presented showing valid results up to a frequency of 2 Hz in high turbulence conditions. Additionally, spatially horizontal distributed measurements with multiple UAS are examined in a case study of a gust front event.

1. Introduction

One of the major challenges in the science of wind energy is the understanding of micro-scale flow conditions within a wind farm [1]. A variety of measurement techniques exist, which qualify for studying the wind conditions in the inflow and wake of wind turbines (WT). Among these are meteorological masts [2], Doppler wind lidar (DWL) [3], or manned [4] as well as unmanned [5] airborne in-situ measurements. All of these systems provide wind measurements with good accuracy, but they are all limited in the flexibility to measure at multiple positions at the same time. We established a system to achieve simultaneous spatial measurements with a fleet of multirotor UAS, the so-called SWUF-3D fleet (Simultaneous Wind Measurements with Unmanned Flight systems in 3D). The major benefit of this approach is, that true simultaneous measurements can be achieved without the need of expensive infrastructure, such as masts or multiple DWL. A possible scenario which thus becomes available for wind energy research is the in-situ measurement of 2-D flow fields of the inflow and wake of a wind turbine.

For single UAS multirotor wind measurement, different approaches exist. First, external wind sensors can be installed at the UAS, such as sonic anemometers [6],[7],[8] or hot wire probes [9],[10]. The second approach is based on the on-board avionic sensors of UAS and relates the

motion of the UAS to the wind [11, 12, 13, 14, 15]. The advantage of an additional wind sensor on the UAS is that theoretically, small scales can be resolved more accurately. However, the motion of the UAS and the disturbance of the wind by the induced air flow from the rotors need to be considered. The additional payload also decreases the flight time. The abdication of additional wind sensors reduces the complexity of the system, which becomes relevant by scaling towards a fleet of UAS measurement devices. Therefore, in the present study the second approach is preferred. The developed algorithm to obtain horizontal wind speed and direction is designed for hovering conditions and is based on the principle of aerodynamic drag and the related quadrotor dynamics. In Sect. 2, the experiment, the improved wind algorithm and the strategy for fleet operation are explained. Section 3 shows the results of the validation of the wind algorithm, temporal resolution of measurements with single UAS and a case study of the fleet measurement within a gust front.

2. Methodology

At the boundary layer field site (Grenzschichtmessfeld, GM) Falkenberg of the Meteorological Observatory Lindenberg - Richard Aßmann-Observatory (MOL-RAO), two campaigns were carried out associated to the FESST@MOL 2020 and the FESSTVaL 2021 activities at the MOL-RAO. With data from the FESST@MOL 2020 experiment, we compared the spatial distribution of horizontal wind in main wind direction, as obtained from the UAS fleet to tower vertical profiles and DWL scans before [16]. In order to calculate turbulence parameters which are essential to understand loads and wake dynamics of WT, it is desirable to measure with high temporal resolution in all three dimensions. In the next step of development in this study, we extend the wind algorithm by the lateral wind component. We also focus on second order statistics and improve the accuracy and temporal resolution by taking additional sensor data into account.

2.1. Experiment description

In June/July 2021 the UAS fleet was deployed for two weeks within the FESSTVaL (Field Experiment on submesoscale spatio-temporal variability in Lindenberg) campaign at MOL-RAO. The data presented in this study was collected during this period. Our goal for the campaign was the calibration and validation of the fleet, and additionally the investigation of turbulence structures with spatially distributed measurements. On the map of the field site in Fig. 1, the 99 m met mast and the different flight pattern, consisting of multiple UAS, are marked. In the map, only the designated measurement positions of the UAS in the hovering state are marked, excluding the flight path from take-off and towards landing. In wind directions between $330-50°$ flow distortion from the tower corrupts the sonic measurements. These directions were excluded from the dataset. For more details on the facilities of the measurement site we refer to Neisser et al. (2002) [17]. In order to calibrated and validate the UAS fleet, we operated multiple UAS in the corresponding altitudes of the sonic anemometer measurements in 50 m and 90 m altitude. In the "calibration pattern", as illustrated in the map in Fig. 1, the UAS are horizontally distributed perpendicular to the dominant wind direction which is from the west in this campaign. Due to safety considerations with regard to mast instrumentation and UAS, the horizontal distance of the UAS to the tower is restricted to a minimum of 20 m. Additionally, in this study we will discuss flights from the "horizontal pattern", with the purpose of turbulence structure analysis. During the complete campaign the UAS are operated in the weather vane mode, which controls the yaw angle in order to orientate the quadrotor towards the wind direction. This feature simplifies and increases the accuracy of the wind algorithm, due to more similar relative inflow of the wind towards the quadrotor, resulting in less variability of the aerodynamic drag. The hardware and software have not changed significantly compared to the 2020 campaign so that we refer to Wetz et al. (2021) [16] for more details.

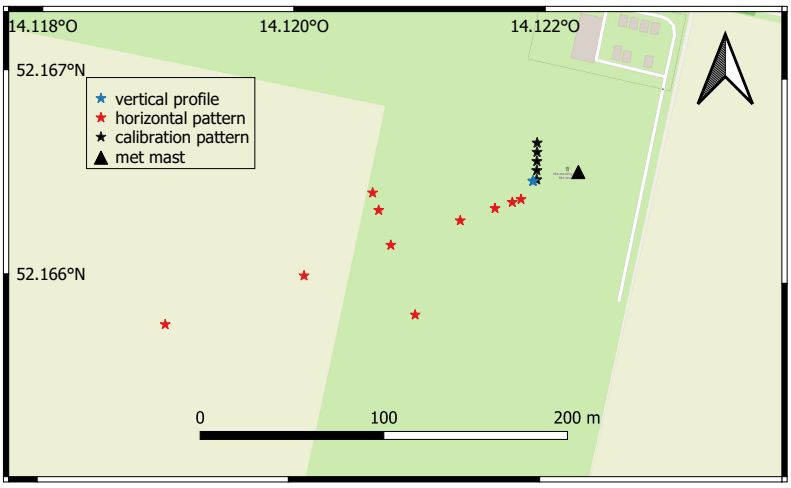

Figure 1. Map of the field site of Falkenberg including the 99 m met mast and different flight patterns of the UAS-fleet. Each star representing an individual UAS at its measurement position. The dark green area is short cut grass, whereas the light green area was a cornfield in 2021. Background map ©OpenStreetMap contributors 2022. Distributed under a Creative Commons BY-SA License.

2.2. Basic equations of quadrotor dynamics

The basis for the calculation of the horizontal wind vector from multicopter data is the equation of motion in longitudinal (x) Eq. (1) and lateral (y) direction Eq. (2) in the body frame of the UAS. Here, g represents the acceleration due to gravity and m the mass of the UAS. The position vector $\mathbf{X_b}$ of the UAS is defined in Eq. (3), the angular velocities $\omega_\mathbf{b}$ and the vector of attitude angles $\mathbf{\Phi_i}$, also known as Euler angles, are defined in Eq. (4) and Eq. (5) respectively. The Euler angles are defined as rotation around the longitudinal axis represented by roll angle ϕ, around the lateral axis as pitch angle θ and around the vertical axis as yaw angle ψ. The wind forces are defined as $\mathbf{F_w}$ in the corresponding directions, x represents the longitudinal and y the lateral direction in the body frame.

$$m(\ddot{x} + q\dot{z} - r\dot{y}) = -mg[\sin(\theta)] + F_{\mathrm{w,x}} \quad (1)$$

$$m(\ddot{y} + p\dot{z} - r\dot{x}) = -mg[\cos(\theta)\sin(\phi)] + F_{\mathrm{w,y}} \quad (2)$$

$$\mathbf{X_b} = \begin{bmatrix} x & y & z \end{bmatrix}^T \quad (3)$$

$$\omega_\mathbf{b} = \begin{bmatrix} p & q & r \end{bmatrix}^T \quad (4)$$

$$\mathbf{\Phi_i} = \begin{bmatrix} \phi & \theta & \psi \end{bmatrix}^T \quad (5)$$

In a first approach the wind forces were calculated according to Wetz et al. (2021) [16], assuming zero motion of the UAS during hovering (see Eq. (6)). In this case, the wind forces are only a function of the Euler angles. The wind forces lateral to the orientation of the UAS are calculated from the roll angle ϕ and the pitch angle θ (Eq. (7)). We now consider the dynamic part of the equation of motion to not be negligible, even in the hover state, but acceleration of the UAS is taken into account for the calculation of the horizontal wind forces (Eq. (8)). Through this, we attempt to increase the accuracy of the wind algorithm especially in the small scales with a better representation of the dynamic behaviour of the UAS. In particular, the linear acceleration in longitudinal and lateral body direction is considered. The accelerometer of the

inertial measurement unit (IMU) measures the acceleration of motion in the three body axis, including the acceleration due to gravity. Alternatively, the derivative of the UAS velocity in the earth frame, as measured by GPS, can be used as linear acceleration after the transformation to the body frame of the UAS. The contribution of gyroscopic terms in Eq. (1,2) is still negligible, since the variances of those terms are two orders of magnitude smaller than the variance of the linear acceleration.

$$F_{\mathrm{w,h,x}} = mg[\sin(\theta)] \tag{6}$$
$$F_{\mathrm{w,h,y}} = mg[\cos(\theta)\sin(\phi)] \tag{7}$$

$$F_{\mathrm{w,x}} = m[g\sin(\theta) + \ddot{x}] \tag{8}$$
$$F_{\mathrm{w,y}} = m[g\cos(\theta)\sin(\phi) + \ddot{y}] \tag{9}$$

The different approaches for the wind forces calculation are compared in Fig. 2a). In this figure the power spectrum density of the forces from the first approach, using only the Euler angles (Eq. 6), are compared with the second approach including linear acceleration (Eq. 8), derived from GPS data ($F_{\mathrm{w,x,g}}$) and from the accelerometer ($F_{\mathrm{w,x,a}}$). The spectral densities are averaged over frequency bins for better visualisation in the figure. The unfiltered data is shown in light grey. The spectrum shows that the wind forces, calculated from the Euler angles of the internal extended Kalman filter (EKF) attitude estimation, follows the theoretical slope of $k^{-5/3}$ Kolmogorov's-law in the inertial subrange of turbulent flows only until approximately 0.5 Hz. The extended Kalman filter (EKF) of the autopilot estimates the dynamic states of the UAS through sensor fusion of inertial and navigation data. However, in this process there are also filters applied to the data. The shape in smaller scales of the Euler angles indicates prior internal filtering of the sensor data. The spectrum of the accelerometer data are aligned to Kolmogorov's-law until 2 Hz, within higher frequencies the noise level dominates. The GPS data show similar behaviour but deviate from the $k^{-5/3}$-slope at 2 Hz already significantly. Due to this, we focus on sensor data from the accelerometers for further processing.

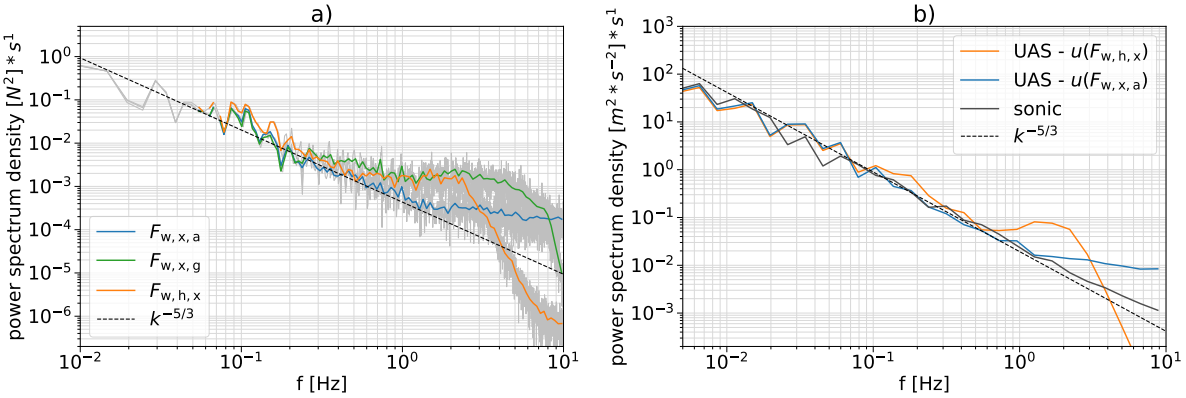

Figure 2. Power spectrum density in longitudinal direction - a) of the wind forces: $F_{\mathrm{w,h,x}}$ hover state assumption, $F_{\mathrm{w,x,a}}$ including acceleration from the accelerometer, $F_{\mathrm{w,x,g}}$ including acceleration from the derived GPS velocity; b) of the wind velocity for different algorithm approaches of UAS measurements in comparison with sonic anemometer data (flight case no. 1 in Table 2).

Table 1. Specification of wind algorithm parameters (proportional parameter c and exponent b).

direction	c	b
longitudinal (x)	7.775	0.845
lateral (y)	6.373	0.898

2.3. Wind vector calibration

The horizontal wind vector $\mathbf{V}$ in the body frame is calculated from the horizontal wind forces using the relationship as described in Eq. (10). In this work, we choose an approach with an unknown exponent b for calibration in contrast to previous work where the Rayleigh drag equation was chosen, which yields $b = 0.5$. The composition of aerodynamic drag of quadrotors is complex, besides the profile and friction losses of the UAS frame, a dominant part of the drag results from the rotor dynamics [18]. The approximation of the relation between wind forces and wind speed with a variable exponent allows, in this case, a more accurate approximation of the calibration curve than the Rayleigh drag equation.

$$\mathbf{V} = \begin{pmatrix} u \\ v \end{pmatrix} = \begin{pmatrix} c_x \cdot F_{\mathrm{w,x}}^{b_x} \\ c_y \cdot F_{\mathrm{w,y}}^{b_y} \end{pmatrix} - \begin{pmatrix} \dot{x}_{gps} \\ \dot{y}_{gps} \end{pmatrix} \tag{10}$$

The calibration dataset consists of 119 calibration flights from the two weeks of the campaign. This includes wind speed ranges from almost 0 up to 8 ms^{-1} with turbulent kinetic energy (TKE) levels from 0.03 to 2.5 $\mathrm{m}^2\mathrm{s}^{-2}$. As it can be seen from Fig. 2, the data are corrupted by noise in the small scales, so that in post-processing, the measurement data are low-pass filtered at 2 Hz in the frequency domain. For the calibration of the wind speed in the body system, the horizontal wind vector is divided into a longitudinal and lateral component aligned to the orientation of the UAS. The calibration target values for the longitudinal wind component are 2 s average wind speeds of the corresponding sonic anemometer measurements. The short average time compared to Wetz et al. (2021) [16] is chosen for better statistics in the calibration of the velocity variance. First, the proportional parameter c_x and the exponent b_x of Eq. (10) are calculated for one specific UAS with the widest range of calibration flights. Similar to previous work, we assume equivalent aerodynamic behaviour within the UAS fleet, so that the calculated parameters for one UAS are valid for the complete UAS-fleet. The calibrated parameters are listed in Table 1. Additionally, offset values for the input parameter pitch $\Delta\theta$, respectively the acceleration Δa, are individually calculated for each UAS of the fleet with only one flight per UAS. The difference between the approaches assuming hover state on the one hand and taking accelerometer data into account on the other hand is shown in the time series of the longitudinal velocity in Fig. 3. It is noticeable that some peaks, that are pronounced with the hover state assumption, are reduced with the acceleration approach, which thus reproduce the dynamic behavior of the reference measurement more realistically. This behaviour can be confirmed with the power spectrum of the longitudinal velocity in Fig. 2, where an overestimation of the energy level in the small scales is visible.

For the calibration of the parameter in lateral direction, the variance σ_v^2 of the single flights is chosen as target value. The mean value of the lateral wind component is not expedient because of the weather-vane mode, which orientates the UAS in wind direction and thus leads to only small absolute values of the lateral wind speed v. Identical to the calibration of the longitudinal wind component, the parameters c_y and b_y are first calibrated for a single UAS and individual offsets for the roll angle are determined for each UAS in a further step. For both directions, the wind estimation is corrected with the UAS velocity measured by the GPS-System ($\dot{x}_{gps}, \dot{y}_{gps}$). Due to the hover state, the magnitude of the GPS velocity is small and only has a minor influence

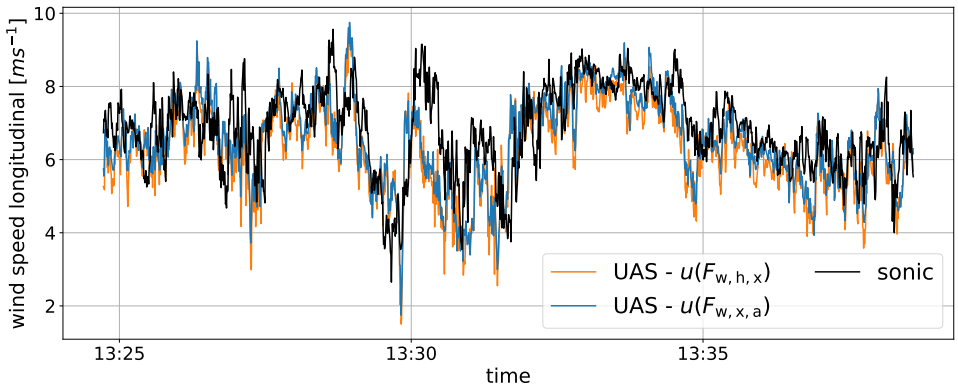

Figure 3. Time series of the longitudinal wind velocity for different algorithm approaches of UAS measurements in comparison with sonic anemometer data - $F_{\mathrm{w,h,x}}$ hover state assumption, $F_{\mathrm{w,x,a}}$ including acceleration from the accelerometer (flight case no. 1 of Table 2).

on the results in some peaks of the GPS velocity (max $|\mathrm{v_{gps}}| = 0.3$ ms^{-1}, $\sigma_{\mathrm{gps}} < 0.003$ m^{2}s^{-2}). In order to rotate the body-frame wind speeds into the geodetic coordinate system, the yaw angle ψ of the UAS is crucial and also needs an offset calibration due to possible errors in the initial calibration of the magnetometers on site. An individual yaw angle offset $\Delta\psi$ for each UAS is calculated from the difference to the reference wind direction which is calculated from the sonic anemometers (Eq. 11). The wind direction in the geodetic frame Φ_w is the corrected yaw angle ψ_c plus the misalignment of the UAS towards the wind direction, which can be calculated as the tangent of the lateral v and longitudinal wind component u in the body frame (Eq. 12). In Fig. 4 the results of the different steps of the wind direction calculation are shown in comparison to reference measurements. It is clearly visible that the dynamic behaviour of the final wind direction calculation follows the reference measurement best. For that particular flight the standard deviation σ of the corrected yaw angle results in $\sigma_{\psi,\mathrm{c}} = 9.0°$, whereas the corrected wind direction yields $\sigma_{\Phi,\mathrm{w}} = 12.1°$, which confirms the improved dynamic behaviour in comparison to the sonic measurements $\sigma_{\Phi,\mathrm{w,sonic}} = 12.5°$.

$$\psi_c = \psi + \Delta\psi \tag{11}$$
$$\Phi_w = \psi_c + \tan(v/u) \tag{12}$$

2.4. Fleet operation

During the campaign we managed to operate 20 UAS simultaneously. The fleet is controlled by a ground station, which is connected to the fleet of UAS through Wifi. Besides the monitoring of the fleet, the ground station operator can also initiate contingency and emergency procedures through the software. Two further remote pilots are employed to observe a maximum of 10 UAS and report unusual behaviour. They can also take control of single UAS if necessary. The specific mission flight patterns for each UAS are planned and uploaded prior to operation. The patterns are generated semi-automatically in order to be able to update the pattern on short notice. This allows the adaption of the mission to current atmospheric conditions, as it was practiced with the "horizontal pattern" to study the turbulence at distributed points along and perpendicular to the main wind direction. With the current setup the flight time for a single UAS is approximately limited to 15 minutes and measurement time needs to be adapted according to the distance of the hover positions to the take-off location, which defines the flight time including.

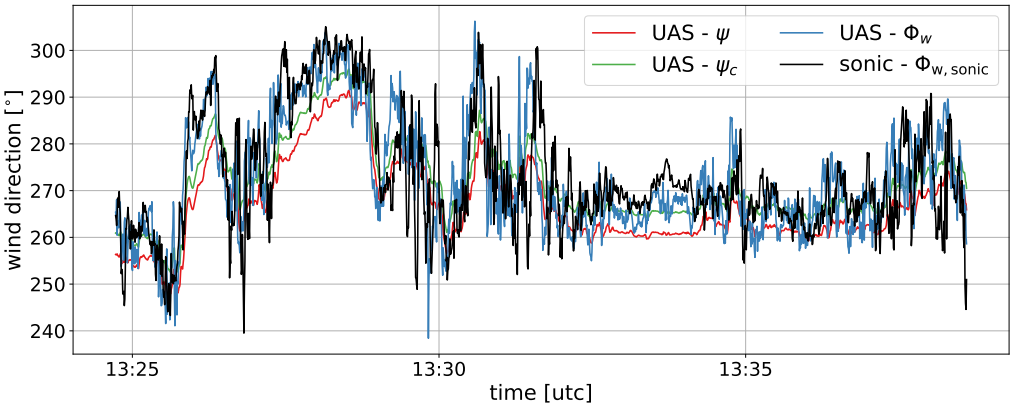

Figure 4. Time series of wind direction for different algorithm approaches of UAS measurements in comparison with sonic anemometer data (flight case no. 1 of Table 2) [ψ: raw yaw angle, ψ_c: calibrated yaw angle, Φ_w: calibrated and with the lateral wind speed corrected wind direction].

However, the measurement time can be significantly increased by replacing the current UAS at the measurement position by a fully charged UAS in flight. If an overlap at the measurement position is guaranteed, continuous measurements at multiple position can be realized. During the campaign, we thus performed vertical profile measurements at five height levels for more than 4 hours continuously during a morning transition of a convective boundary layer. Furthermore, a measurement time of more than 40 min with the "horizontal pattern" was achieved by replacing 10 UAS twice.

3. Results

3.1. Calibration

In order to produce reliable calibrations and quantification of the measurement accuracy, we performed calibration flights with each UAS of the fleet at different atmospheric conditions. The results of 119 single UAS calibration flights are shown in the scatter plots in Fig. 5. The measurement data used for the calibration are excluded in the results to ensure an independent dataset for the validation of the UAS fleet. Each data point represents the time average of one flight versus the sonic anemometer average for the same time. The wind vector is calculated with the improved algorithm including the accelerometer data. In Fig. 5a, the mean longitudinal velocity of the UAS measurement is shown to be in good agreement with the reference in a broad range of wind speeds. A mean RMSE of $\epsilon_u = 0.25$ ms^{-1} is achieved. Compared to the approach with the hover state assumption (RMSE of $\epsilon_u = 0.3$ ms^{-1}), the accelerometer approach could increase the accuracy. In particular, the accuracy of the wind speed variance (Fig. 5b) with an RMSE of $\epsilon_{\sigma^2,\mathrm{u}} = 0.16$ m^{2}s^{-2} is improved significantly. Furthermore, the variance of the lateral wind component is reproduced with an RMSE to the reference measurement of $\epsilon_{\sigma^2,\mathrm{v}} = 0.08$ m^{2}s^{-2} (Fig. 5c). The additional correction of the wind direction with the lateral and longitudinal wind component results in an average RMSE of less than $\epsilon_{\Phi,\mathrm{w}} < 5°$ (Fig. 5 d).

3.2. Turbulence analyses

To evaluate the performance of the UAS measurements in different atmospheric conditions and especially with regards to their capabilities to resolve turbulence, four different flights are examined in more detail. The cases were selected in order to cover a range of possible different atmospheric conditions, from stable to unstable atmospheric stratification, high and low turbulence. Flight no. 1 was performed during convective conditions in the late afternoon.

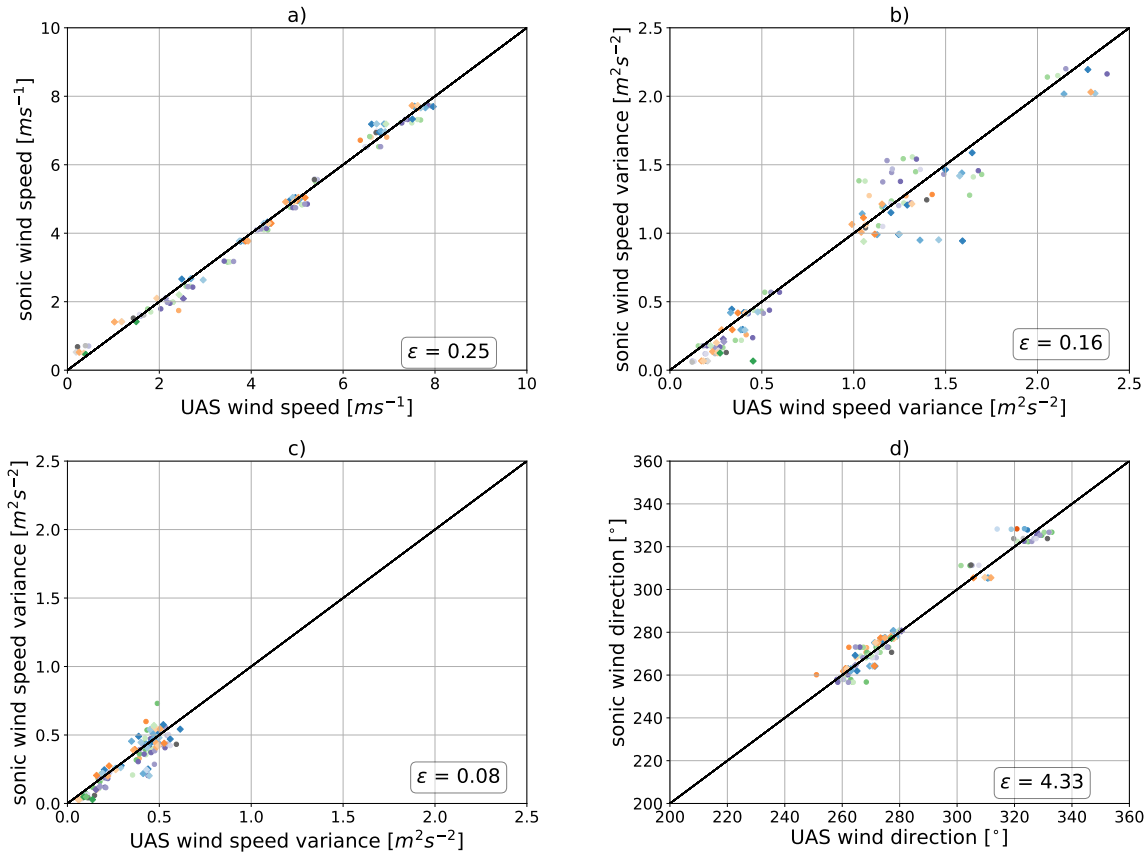

Figure 5. Flight averaged data for all calibration flights, different colors and markers representing different UAS (no. 2-35) measurements in comparison to sonic anemometer wind measurements including the RMSE ϵ : a) longitudinal wind speed, b) longitudinal wind speed variance, c) lateral wind speed variance, d) wind direction.

Table 2. Specification of four case studies (mean horizontal wind speed $\overline{V_w}$, horizontal variance $\sigma^2_{\mathrm{u,v}}$).

case no.	date	time [utc]	$\overline{V_w}$ [ms^{-1}]		$\sigma^2_{\mathrm{u,v}}$ [m^{2}s^{-2}]		characterisation
			sonic	UAS	sonic	UAS	
1	02/07/2021	13:22	6.88	6.54	2.01	1.89	convective
2	30/06/2021	14:57	7.27	7.21	1.73	1.65	shear turbulence
3	28/06/2021	3:54	6.76	6.49	0.15	0.17	low level jet
4	26/06/2021	9:50	1.64	1.74	0.10	0.24	low wind speed

A high level of turbulence is present in flight no. 2 which is however more shear-driven. The mean wind speed during the morning transition in flight no. 3 was high due to a low level jet event at the top of the nighttime inversion layer, but the turbulence intensity in the LLJ is significant smaller than in case 1 and 2 due to the strong static stability. The last case, flight no. 4, represents a day with very low wind speeds. The different flights and the respective wind speed and turbulence conditions in the form of horizontal wind speed variance $\sigma^2_{\mathrm{u,v}}$ are listed in Table 2. The comparison of the power spectrum density of horizontal wind speed between the four flight cases in Fig. 6 demonstrates the different turbulence conditions during the flights.

Case no. 1 and 2 with high turbulence levels show a pronounced inertial subrange that follows the Kolmogorov-law within the regarded scales up to 2 Hz. In contrast, the low turbulence cases no. 3 and 4 show that in such conditions even the sonic anemometer spectra are flatter than $k^{-5/3}$. As emphasized in section 2.3, the UAS sensors are limited in resolving small scales. This limitation is more pronounced in low turbulence conditions, where the energy level of the complete spectrum is lower. The noise level of the UAS data has an almost constant energy density level of about 0.01 $\mathrm{m^2 s^{-1}}$, which results in an additional variance of $\sigma^2_{\mathrm{noise}} \approx 0.1\ \mathrm{m^2 s^{-2}}$ assuming a constant noise level in the complete frequency domain. Therefore, in low turbulence condition the noise of the sensor dominates even at lower frequencies and corrupts the turbulence measurement. The case studies outline that in conditions with wind speed variances of the order of 0.3 $\mathrm{m\,s^{-1}}$ or smaller, the resolution of turbulence is not possible with the current system. The temporal resolution in low wind speed could potentially be improved by more accurate accelerometers, or by the reduction of the noise level due to vibration of the system. Additionally, the dimension of the quadrotor limits the resolvable scales, such that even smaller multicopters could lead to improved temporal resolution regarding the small scales.

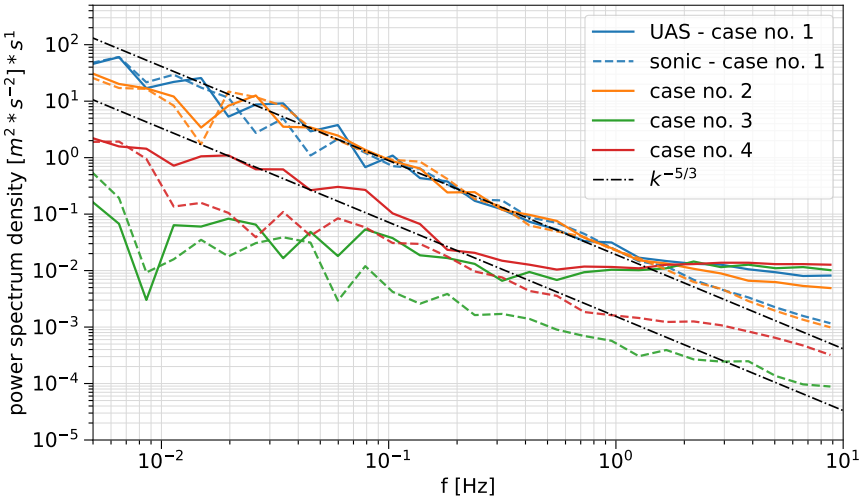

Figure 6. Power spectrum density of the wind velocity measurement from the UAS and the corresponding sonic anemometers for the four defined flight cases. Solid lines represent UAS measurements, dashed lines sonic anemometer measurements.

3.3. Distributed measurements in a gust front

In addition to the calibration flights, one flight of the horizontal pattern is shown in Fig. 7. In that flight, ten UAS hovered at 50 m AGL while a gust front, associated to a convective cell approximately 8 km east of the site, hit the site with wind speeds up to 15 $\mathrm{m^2 s^{-2}}$. In the map, each UAS with its measured wind vector is drawn at the time marked in the time series below with the green vertical line. The gust from the east approaches the UAS pattern and appears first at the sonic anemometer (black arrow) and UAS #22 (blue) in the east before it reaches the most western UAS #28 (red) with a delay of almost 20 s. This corresponds to an advection velocity of 10 $\mathrm{m^2 s^{-2}}$ for the 200 m distance between the quadrotors. Considering a WT with a rotor diameter of 100 m at the location of UAS #28, the UAS are distributed in wind direction in an area corresponding to two rotor diameters (2 D), and at a distance of 1 D, three more UAS are positioned perpendicular to the wind direction. It is obvious that the flow field is far from uniform during an event like this. This demonstrates the challenges for WT controllers and

the corresponding operational wind measurement systems, e.g. lidars, to provide a meaningful control variable. A more detailed analysis of the flow structure during this event is beyond the scope of this paper, but will be presented in a future publication.

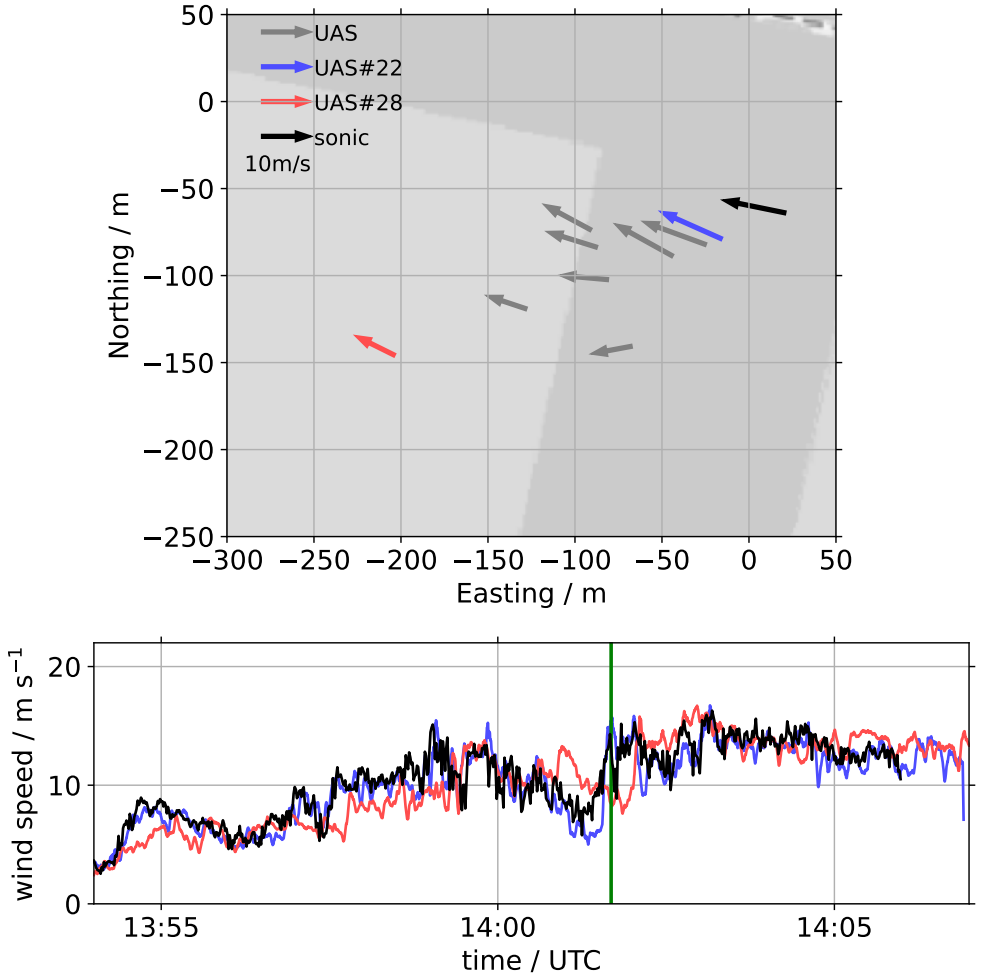

Figure 7. Time series of horizontal wind speed measurements during an incoming gust front of a cold pool event for the horizontal flight pattern. The map shows the distributed measurements of the wind vector of 9 UAS hovering at 50 m (light grey, blue and red). The time series below gives the corresponding horizontal wind speeds for the two outermost quadrotors and the sonic anemometer at the meteorological mast.

4. Conclusions

Within a two-week campaign in summer 2021, we demonstrated the capability of the SWUF-3D UAS fleet to measure the horizontal wind vector with high temporal resolution at spatially distributed measurement points. The improvement and the extension of the wind algorithm compared to previous versions is demonstrated. Besides the adapted calibration for improvements of variance measurements, the calculation of the lateral wind component is introduced. That enables additional corrections of the wind direction, which particularly improved the dynamic response of the measurement. Overall, the revised algorithm results in an RMSE of $\epsilon_{\overline{u}} =$

0.25 ms^{-1} for the mean wind speed of 119 calibrations flights and $\epsilon_{\sigma^2,\mathrm{u}} = 0.16\ \mathrm{m}^2\mathrm{s}^{-2}$ for the RMSE of the variance. Additionally, a high accuracy for the wind direction is achieved with an RMSE of $\epsilon_{\Phi,\mathrm{w}} < 5°$.
The capabilities and limitations of the measurement system for turbulence measurements are demonstrated with four exemplary cases. We show that there is a lower limit of the scales that can be resolved with the SWUF-3D quadrotors. Limitations by sensor noise and rotor induced flow distortion do not allow a good resolution of the turbulence spectrum in conditions with wind speed variances of the order of 0.3 $\mathrm{m\,s}^{-1}$ or smaller and at frequencies higher than 2 Hz. This is especially critical in stable atmospheric conditions where turbulence is generally low and intermittent. For applications which are most relevant for wind energy production, the measurements by the fleet and its resolvable scales can be of great benefit to analyse inflow and wake of WTs. Furthermore, the capability of accurate wind measurements in a broad range of wind velocities during gusty conditions is demonstrated with a horizontal flight pattern during the FESSTVaL campaign. This particularly shows the spatial variability of the flow during such an event, with possible implications for WT loads and control.

Acknowledgments

We thank Josef Zink for his contribution and May Bohmann for her assistance to the FESSTVaL experiment. Furthermore, we thank the Hans Ertel Centre for Weather Research (HErZ) of DWD for the invitation and organisation of the FESSTVaL campaign and particularly Frank Beyrich for the relentless local support and the provision of measurement data of the GM Falkenberg.

References

[1] Veers P, Dykes K, Lantz E *et al.* 2019 *Science* **366** eaau2027
[2] Rajewski D A *et al.* 2013 *Bulletin of the American Meteorological Society* **94** 655–672 ISSN 0003-0007
[3] Wildmann N *et al.* 2018 *Atmospheric Measurement Techniques* **11** 3801–3814
[4] Platis A, Siedersleben S K, Bange J, Lampert A, Bärfuss K, Hankers R, Cañadillas B, Foreman R, Schulz-Stellenfleth J, Djath B, Neumann T and Emeis S 2018 *Scientific Reports* **8** 2163
[5] Wildmann N, Hofsäß M, Weimer F, Joos A and Bange J 2014 *Advances in Science and Research* **11** 55–61
[6] Shimura T, Inoue M, Tsujimoto H, Sasaki K and Iguchi M 2018 *Journal of Atmospheric and Oceanic Technology* **35** 1621–1631
[7] Thielicke W, Hübert W, Müller U, Eggert M and Wilhelm P 2021 *Atmospheric Measurement Techniques* **14** 1303–1318
[8] Reuter M, Bovensmann H, Buchwitz M, Borchardt J, Krautwurst S, Gerilowski K, Lindauer M, Kubistin D and Burrows J P 2021 *Atmospheric Measurement Techniques* **14** 153–172
[9] Cuxart J, Wrenger B, Matjacic B and Mahrt L 2019 *Atmosphere* **10** 715
[10] Christian M and Po Wen C 2020 *Journal of Physics: Conference Series* **1618** 032049
[11] Palomaki R T, Rose N T, van den Bossche M, Sherman T J and Wekker S F J D 2017 *Journal of Atmospheric and Oceanic Technology* **34** 1183–1191
[12] Neumann P, Asadi S, Lilienthal A, Bartholmai M and Schiller J 2012 *IEEE Robotics & Automation Magazine* **19** 50–61
[13] González-Rocha J, Woolsey C A, Sultan C and Wekker S F J D 2019 *Journal of Guidance, Control, and Dynamics* **42** 836–852
[14] Brosy C, Krampf K, Zeeman M, Wolf B, Junkermann W, Schäfer K, Emeis S and Kunstmann H 2017 *Atmospheric Measurement Techniques* **10** 2773–2784
[15] Bell T M, Greene B R, Klein P M, Carney M and Chilson P B 2020 *Atmospheric Measurement Techniques* **13** 3855–3872
[16] Wetz T *et al.* 2021 *Atmospheric Measurement Techniques* **14** 3795–3814
[17] Neisser J, Adam W, Beyrich F, Leiterer U and Steinhagen H 2002 *Meteorol. Z. (N.F.)* **11** 241–253
[18] Sun S, De Visser C and Chu Q 2018 *Journal of Aircraft* **56** 1–17